Open Access

Earth System
Science
Data

Discussions

1
2
3
4 **Expanding understanding of optical variability in Lake Superior with a four-year dataset**
5
6
7 Colleen B. Mouw[1*], Audrey B. Ciochetto[1], Brice Grunert[2], Angela Yu[2]
8
9
10
11 [1]University of Rhode Island, Graduate School of Oceanography
12 215 South Ferry Road
13 Narragansett, RI 02882
14 USA
15
16 [2]Michigan Technological University
17 1400 Townsend Drive
18 Houghton, MI 49931
19 USA
20
21
22 [*]Corresponding author, cmouw@uri.edu, +1 401-874-6506
23
24

25   **Abstract**

26   Lake Superior is one of the largest freshwater lakes on our planet, but few optical observations

27   have been made to allow for development and validation of visible spectral satellite remote

28   sensing products. The dataset described here focuses on coincidently observing inherent and

29   apparent optical properties along with biogeochemical parameters. Specifically, we observe

30   remote sensing reflectance, absorption, scattering, backscattering, attenuation, chlorophyll

31   concentration, and suspended particulate matter over the ice-free months of 2013-2016. The

32   dataset substantially increases the optical knowledge of the lake. In addition to visible spectral

33   satellite algorithm development, the dataset is valuable for characterizing the variable light field,

34   particle, phytoplankton, and colored dissolved organic matter distributions, and helpful in food

35   web and carbon cycle investigations, among others. The compiled data can be freely accessed

36   at: https://seabass.gsfc.nasa.gov/archive/URI/Mouw/LakeSuperior/.

37

1. Introduction

Lake Superior is the largest of the Laurentian Great Lakes, the largest lake on Earth by area and third largest lake on Earth by volume. Direct observations of Lake Superior are rare for nearly half of the year due to the long winter climatic conditions of the region. *In situ* observations are scarce November through April, and in many years October and May are also precluded as seasonal storms and ice coverage hinder ship-based observations for long periods of time. As such, remote sensing is an important observational platform for observing the lake.

Remote sensing of inland and coastal waters requires continued investment in *in situ* sampling to fully capture the dynamic range of parameter values and shifting relationships due to response to climate change (Dierssen 2010), anthropogenic stress, and invasive species (Mouw et al., 2015). Remote sensing efforts on the lake initially focused on estimating chlorophyll concentration with band-ratio algorithms (Budd and Warrington, 2004; Li et al., 2004) and met with limited success. More recently, Mouw et al. (2013) evaluated a variety of semi-analytical algorithms to identify the best performing for refinement. They found the retrieval of chlorophyll concentration was not possible via inversion since errors in derived colored dissolved organic matter (CDOM) absorption were greater than the total contribution of phytoplankton to the overall absorption budget. However, they did demonstrate success in retrieving absorption due to CDOM. In light of the challenge to retrieve chlorophyll concentration, Trochta et al. (2015) classified remote sensing reflectance spectra into optical water types and connected the spatial and temporal variability of the water types to physical processes of the lake.

In situ observations are an essential component of remote sensing satellite algorithm development and validation. At the time that Mouw et al. (2013) completed their evaluation of

61 algorithms, there were only 8 stations with coincident observations of radiometry, absorption,

62 and scattering for Lake Superior (Peng et al., 2009; Effler et al., 2010; O'Donnell et al., 2013).

63 To enable continued development of remote sensing algorithms for Lake Superior, a greater

64 investment in optical observations were needed. Here we describe a dataset of coincident

65 inherent and apparent optical properties collected throughout Lake Superior over the ice-free

66 months of 2013 to 2016. Inherent optical properties (IOPs, i.e. absorption and

67 scattering/backscattering) depend on in-water dissolved and particulate constituents, while

68 apparent optical properties (AOPs, i.e. reflectance and attenuation) are dependent on both in-

69 water constituents and the ambient light field. Collectively, these properties include remote

70 sensing reflectance, absorption, scattering, backscattering, attenuation, pigment concentrations,

71 and total suspended matter. Beyond satellite algorithm development, the dataset is valuable for

72 characterizing the variable light field, particle, phytoplankton, and colored dissolved organic

73 matter distributions, and helpful in food web and carbon cycle investigations, among others.

74

75 **2. Data and Methodology**

76 *2.1   Study Site*

77   Containing approximately 10% of the Earth's surface freshwater, Lake Superior (Figure

78 1) is the largest freshwater body on the planet by area (8.21×10^4 km^2) and third largest by

79 volume (1.21×10^4 km^3). The cold temperatures and low nutrient concentrations of Lake

80 Superior (Sterner, 2011), compared to the other Laurentian Great Lakes, result in oligotrophic

81 conditions (e.g. Matheson and Munawar, 1978; Munawar and Munawar, 1973; Weller, 1978;

82 Barbiero and Tuchman, 2001) with low primary production (Sterner, 2010) and low species

83 richness (Hubbs and Lagler, 2004). Superior is the fastest warming of all the Great Lakes

84   (Mason et al., 2016), with summer surface temperatures rising faster than the temperature of the

85   surrounding atmosphere (Austin and Allen, 2011; Austin and Colman, 2007; Lenters, 2004).

86   This trajectory puts Lake Superior close to the upper range of global lake warming trends

87   (O'Reilly et al., 2015). These warming trends impact the lake's energy balance, hydrology, ice

88   cover, and mixing dynamics, which in turn impacts biotic and biogeochemical responses. The

89   previous limited optical observations of Lake Superior reveal that light absorption is dominated

90   by colored dissolved organic matter (CDOM; $\geq 75\%$ of the total absorption at 440 nm) (Effler et

91   al., 2010) and the majority of the backscattering in the lake is attributed to organic rather than

92   minerogenic sources (Peng et al., 2009).

93   *2.2   In Situ Optical Observations*

94   Optical and biogeochemical data are collected in Lake Superior during the ice-free

95   months (May – October) of 2013 through 2016 (Figure 1). The dataset consists of a full suite of

96   coincident IOPs and AOPs. Observed IOPs include absorption due to water itself ($a_w(\lambda)$, m^{-1}),

97   phytoplankton ($a_{ph}(\lambda)$, m^{-1}), non-algal particles ($a_{NAP}(\lambda)$, m^{-1}), colored dissolved organic matter

98   ($a_{CDOM}(\lambda)$, m^{-1}), and backscattering due to water itself ($b_{bw}(\lambda)$, m^{-1}) and particles ($b_{bp}(\lambda)$, m^{-1}).

99   Observed AOPs include downwelling and surface irradiance ($E_d(\lambda)$ and $E_s(\lambda)$, respectively, μW

100   cm^{-2}) along with upwelling radiance ($L_u(\lambda)$, μW cm^{-2} sr^{-1}), which are used to retrieve remote

101   sensing reflectance ($R_{rs}(\lambda)$, sr^{-1}) and downwelling and upwelling diffuse attenuation coefficients

102   ($K_d(\lambda)$ and $K_u(\lambda)$, m^{-1}, respectively). A summary of parameters and units can be found in Table

103   1.

104   *2.2.1   Apparent Optical Properties*

105   Radiometric measurements are made with three HyperOCR spectral radiometers

106   (Satlantic Inc.) that measure between 350–800 nm with approximately 3 nm resolution (137 total

107   wavelengths). In-water $E_d(\lambda)$ and $L_u(\lambda)$ HyperOCR sensors are attached to a free-falling Profiler

108   II frame (Satlantic Inc.), while the $E_s(\lambda)$ sensor is mounted on top of the ship to allow for

109   correction of the other measurements due to changing sky conditions. At each station, the

110   system is deployed for three cast types: surface, multi- and full profile. To characterize the

111   air/water interface, a floatation collar on the profiler frame enables continuous measurement of

112    $L_u(\lambda)$ approximately 20 cm below the water surface for 5 minutes (surface profile). The flotation

113   collar is removed and the profiler then deployed in free-fall mode, measuring 5 consecutive

114   profiles from the surface to 10 m to characterize the near-surface light field (multi-profile).

115   Finally, the profiler is allowed to free-fall to the 1% light level or to within 10 m of the bottom,

116   whichever is shallower (full profile).

117   All methods and analysis follow the NASA ocean optics protocols for satellite ocean

118   color sensor validation (Mueller et al., 2003a). Briefly, $E_d(\lambda)$, $L_u(\lambda)$ and $E_s(\lambda)$ are dark-corrected

119   and quality controlled to exclude data collected at high instrument tilt (>4º). $E_s(\lambda)$ is smoothed

120   over a 15 s interval and $E_d(t,\lambda)$ and $L_u(t,\lambda)$ normalized to the ratio of $E_s(t_0,\lambda)/E_s(t,\lambda)$ to account

121   for variability in surface irradiance throughout each profile measurement. Data from surface,

122   multi- and full profiles are each binned to 1 m.

123   Using binned multi-profile data, normalized $E_d(z,\lambda)$ and $L_u(z,\lambda)$ are natural log

124   transformed and fit as a function of depth to retrieve attenuation coefficients $K_d(\lambda)$ and $K_u(\lambda)$,

125   respectively (Smith and Baker, 1984; 1986):

126                          $\ln[X(z,\lambda)] = \ln[X(z_m,\lambda)] - (z - z_m)K(z_m)$ (1)

127   where X is either E_d or L_u, z is depth, z_m is a central reference depth and K is either K_d or K_u.

Earth System
Science
Data

Open Access

Discussions

128 This method assumes K is uniform across the depth interval used in the regression. For the

129 majority of the Lake Superior dataset, the upper 8 m of the water column is typically utilized for

130 the retrieval of K, as recommended by Smith and Baker (1984; 1986). However, some locations

131 near river outflows show shallow layers with distinct optical changes, reducing the uniform

132 depth interval to about 5 m.

133 Using K-regression results, $E_d(\lambda)$ and $L_u(\lambda)$ are propagated to just below the surface

134 ($E_d(0^-,\lambda)$ and $L_u(0^-,\lambda)$). Water leaving radiance ($L_w(\lambda)$) is calculated from $L_u(0^-, \lambda)$ according

135 to:

136 $$L_w(\lambda) = 0.543 \cdot L_u(0^-, \lambda) \tag{2}$$

137 where 0.543 accounts for the net effects of surface reflectance and the refractive index of

138 seawater as light travels across the sea/air interface (Lee et al., 2002; Mobley, 1994). $R_{rs}(\lambda)$ is

139 then retrieved as:

140 $$R_{rs}(\lambda) = \frac{L_w(\lambda)}{E_s(\lambda)} \tag{3}$$

141

142 *2.2.2 Inherent optical properties*

143 IOPs are collected via a vertically profiled bio-optical package that measures absorption,

144 attenuation (WET Labs AC-S) and backscattering (WET Labs ECO-BB9) along with concurrent

145 temperature, salinity (SeaBird CTD 37SI) and fluorometeric chlorophyll *a* (WET Labs ECO-

146 FL3). All methods and analysis follow the NASA ocean optics protocols for satellite ocean color

147 sensor validation (Mueller et al., 2003b). The ECO-FL3 is calibrated on a yearly basis,

148 regressing *in situ* chlorophyll *a* fluorescence with extracted chlorophyll *a* concentration ([Chl],

149 mg m^{-3}) derived from discrete field samples.

150   Total absorption and attenuation ($a_t(\lambda)$ and $c_t(\lambda)$, m^{-1}, respectively) are resolved at 81

151   wavelengths between 400-750 nm. CTD data are used to correct $a_t(\lambda)$ and $c_t(\lambda)$ for temperature

152   and salinity effects using the coefficients of Sullivan et al. (2006). The AC-S is calibrated before

153   and after each cruise with ultrapure water (ion, particle, and bubble free). This pure-water

154   absorption and attenuation ($a_w(\lambda)$ and $c_w(\lambda)$) is subtracted to retrieve the contribution of non-

155   water components ($a_{nw}(\lambda)$ and $c_{nw}(\lambda)$). Data are corrected for scattering effects using the

156   proportional method of Zaneveld et al. (1994). The bio-optical package is deployed for two

157   successive casts: total and filtered. For the filtered cast, the AC-S intake is fit with a 0.2 μm

158   filter (PALL, Maxi Capsule Filter 12112) to allow for the measurement of dissolved components

159   only ($a_{CDOM}(\lambda)$, m^{-1}). During deployment, the package is lowered at 0.2 m s^{-1} or as slow as

160   possible. All data are binned to 1-m during analysis. Particulate absorption ($a_p(\lambda)$, m^{-1}) is

161   retrieved by the difference between total and filtered casts ($= a_{nw}(\lambda) - a_{CDOM}(\lambda)$). Pure-water

162   absorption and attenuation as measured by Pope and Fry (1997) is then added to $a_{nw}(\lambda)$ and

163    $c_{nw}(\lambda)$ to return to total values.

164   The ECO-BB9 measures the volume scattering coefficient (β_t, m^{-1} sr^{-1}) for an acceptance

165   angle of 124° at 9 wavelengths: 412, 440, 488, 510, 532, 595, 650, 676 and 715 nm. Instrument

166   calibration was performed at WET Labs in Narragansett, RI using 0.1 μm NIST-traceable beads

167   (Thermo-Scientific, 3100A, bead lot number 43585) at 9°C following the procedure of Sullivan

168   et al. (2013). Processed AC-S measurements are interpolated to BB9 wavelengths and

169   backscattering data corrected for absorption:

170    $$\beta = \beta_t \, e^{(l - a_t)} \qquad\qquad (4)$$

171   where l is the pathlength of the BB9 (=0.0391 m). The volume scattering function (β_w, m^{-1} sr^{-1})

172   and total scattering (b_w, m^{-1}) of pure-water is retrieved from temperature and salinity

173   measurements using the model of Zhang and Hu (2009). Backscattering of pure-water (b_{bw}, m^{-1})

174   is considered half of total scattering ($= b_w/2$). Volume scattering of the particulate fraction (β_p,

175   m^{-1} sr^{-1}) can then be retrieved by difference ($= \beta - \beta_w$). Particulate backscattering is calculated

176   by taking acceptance angle into account (Sullivan et al., 2013):

177    $$b_{bp} = 2\pi \chi \beta_p \qquad (5)$$

178   where χ=1.076 for a 124° measurement angle. Total backscattering (b_b, m^{-1}) can then be

179   retrieved as the sum of particulate and water components ($= b_{bp} + b_{bw}$).

180

181   *2.2 Laboratory Analysis of Discrete Water Samples*

182   Whole water samples are taken from multiple depths representative of the surface (5 m)

183   and at a mid-depth of the euphotic zone often coincident with the deep chlorophyll maximum if

184   one is present (11-50 m). During well-mixed times of year, when a deep chlorophyll layer is not

185   observed, samples are only taken in the surface layer. Collected water is stored in the dark on ice

186   and is processed within 8 hours. Discrete water samples are used for determining [Chl], $a_p(\lambda)$,

187    $a_{NAP}(\lambda)$, $a_{ph}(\lambda)$, $a_{CDOM}(\lambda)$ and the organic and inorganic components of suspended particulate

188   matter (SPM$_O$ and SPM$_I$, mg L^{-1}, respectively).

189   Samples for [Chl] and $a_p(\lambda)$ are filtered in triplicate onto Whatman glass fiber filters

190   (GF/F, 0.7μm nominal pore size), stored in liquid nitrogen while at sea and moved to a -80°C

191   freezer in the lab until analysis. Samples for $a_{CDOM}(\lambda)$ are filtered through an acid-washed 0.2

192   μm membrane filter (Whatmann Nucleopore, 111106) and the filtrate stored in clear borosilicate

193   bottles (Qorpak, GLC-01151) in a refrigerator until analysis. Directly prior to each cruise,

194   borosilicate bottles are acid-washed and muffled at 450°C for 4 hours to remove any potential

195   contaminants.

196   Spectral CDOM, particulate, non-algal and phytoplankton absorption are measured

197   spectrophotometrically (Perkin-Elmer Lambda 35 UV/VIS dual-beam) for wavelengths between

198   300-800 nm. Absorption of CDOM filtrate is measured in a 10-cm cuvette following NASA's

199   Ocean Optics Protocols (Mueller et al., 2003b) using a slit-width of 2 nm and a scan rate of 240

200   nm min^{-1}. For particulate and non-algal absorption, we follow the transmission-reflectance (T-R)

201   method (Tassan and Ferrari ,2002; Lohrenz, 2000; Lohrenz et al., 2003) that utilizes an

202   integrating sphere to correct measurements for the contribution of scattering. Daily blanks are

203   prepared by filtering 25 mL of ultrapure water (ion and particle free) onto a GF/F and used to

204   normalize T-R data during analysis. Filters are placed on a quartz slide at the entrance

205   (transmittance) and exit (reflectance) of the sphere and scanned at a speed of 120 nm min^{-1} with a

206   slit width of 2 nm both before (a_p) and after (a_{NAP}) exposure to sodium hypochlorite. The

207   difference between these measurements is the contribution due to phytoplankton ($a_{ph} = a_p -$

208   a_{NAP}). Absorption is calculated following Lohrenz et al. (2000).

209   Extracted [Chl] and phaeopigments are determined following the NASA Ocean Optics

210   Protocols (Trees et al., 2003) for both instrument calibration and sample analysis. Working in

211   the dark, filtered samples are placed in pre-chilled 90% acetone and sonicated for 20 to 30s to

212   break cells open. Sonicated samples are stored in the freezer (-20°C) and allowed to extract for

213   24 hours prior to analysis. Samples are brought to room temperature and centrifuged at 3000

214   RPM for 20 minutes to remove filter particulates. Fluorescence is measured before and after the

10

215   addition of 50μL of 10% HCl on a Turner Designs 10-AU fluorometer (Optical Kit 10-037R).

216   Blanks of 90% acetone are measured daily. The fluorometer is calibrated yearly with a dilution

217   series of pure chlorophyll a (Sigma-Aldrich C6144) extracted in 90% acetone. Field samples are

218   analyzed within 6 months of fluorometer calibration. [Chl] is retrieved from blank-corrected

219   fluorescence as:

220    $$[Chl] = \frac{(F_b - F_a)}{F_R} \cdot \frac{\tau}{\tau - 1} \cdot \frac{V_S}{V_F} \tag{6}$$

221   and phaeopigment concentration ([Phaeo], mg m^{-3}) calculated as:

222    $$[Phaeo] = \frac{(F_a \tau - F_b)}{F_R} \cdot \frac{\tau}{\tau - 1} \cdot \frac{V_S}{V_F} \tag{7}$$

223   where F_b and F_a (FSU) are fluorescence measured before and after acidification, respectively, F_R

224   (FSU (mg m^{-3})$^{-1}$) is the slope of the fluorometer calibration, τ (unitless) is the acid-ratio of the

225   fluorometer calibration and V_S and V_F (mL) are the volume of solvent and filtered water sample,

226   respectively.

227   Both organic and inorganic SPM are quantified following the methodology of the

228   American Public Health Association, American Water Works Association and Water

229   Environment Federation (2005) and the recommendations of Boss et al. (2009) and Woźinak et

230   al. (2011). Whatman GF/F filters (47mm, 0.7μm pore size) are prepared by washing with

231   ~100mL ultrapure water to rinse away any loose glass fibers. They are then dried at 103-105°C

232   for 1 hour and then muffled at 550°C for 4 hours and allowed to cool in a desiccator. Filters are

233   pre-weighed on a high-precision balance (W_F, mg). Duplicate samples are filtered with a

234   minimum of 3L of collected water and stored at -80°C until analysis. Samples are removed from

235   the freezer, dried at 103-105°C for 1 hour and placed in a desiccator to cool. Dried filters are

236   then weighed within 2 hours of removal from the oven (W_R, mg). Filters are muffled at 550°C

237   for 1 hour, returned to the desiccator to cool and re-weighed (W_I, mg). Total and inorganic SPM

238   are retrieved as:

239    $$SPM = (W_R - W_F)/V \qquad (8)$$

240    $$SPM_I = (W_I - W_F)/V \qquad (9)$$

241   where V is the volume filtered (L). The organic component can be retrieved by difference

242   ($SPM_O = SPM - SPM_I$).

243

244   **3. Results**

245   Data are collected from 106 stations from May through October of 2013 to 2016.

246   Collection is aimed at maximizing spatial and temporal variability and dynamic range. Thus,

247   repeat stations are only found for 6 locations. Most of the observations are made in July (n=29)

248   and August (n=28), but also show reasonable distribution in the early spring (May n=12; June

249   n=8) and fall (September n=16; October n=13). Data are only collected in U.S. waters, thus the

250   Canadian waters encompassing the northern reaches of the lake are not observed. To some

251   extent, sampling locations are dependent on the home-port location of research vessels. The

252   western basin (41%) and the central basin, near the Keweenaw Peninsula (41%) of the lake are

253   well observed. The eastern basin is observed only during July of 2015 and a single site in July

254   2013, August 2014, and September 2013 (Figure 1).

255   The lake is dimictic (Assel, 1986) and develops a strong thermocline and deep

256   chlorophyll maximum (DCM (Barbiero et al., 2004) in the summer months. The water column is

257   completely mixed in May and June of all years (Figure 2 A, B). A thermocline is evident in

258   nearly all locations by July (Figure 2 C), becoming stronger and deeper in August (Figure 2 D).

259   Depending on location and year, the thermocline either deepened or shallowed in September and

260   October, with evidence of a fully mixed water column in some locations in October (Figure 2 E,

261   F). In the fluorometric [Chl] profiles shown in Figure 2, [Chl] is slightly lower in the near

262   surface water in May and June due to fluorescence quenching when the water column is well

263   mixed (Figure 2 G, H). When [Chl] is derived from absorption, the profiles are uniform at this

264   time of the year (not shown). The formation of a DCM follows the development of the

265   thermocline. As the thermocline sets up in July the DCM develops and becomes more

266   pronounced and deeper in August as the thermocline deepens (Figure 2 I, J). The DCM is still

267   evident in September, but becoming weaker in magnitude and beginning to shallow (Figure 2 K).

268   By October, when the lake is beginning to become fully mixed, [Chl] remains low in the near

269   surface waters and slightly elevated in mid-depths where the DCM was previously found (Figure

270   2 L).

271   Discreet absorption samples partitioned into water, phytoplankton, non-algal particles

272   and CDOM display contributions from riverine inputs, and broad lake processes near surface at

273   mid-depth (Figure 3). The St. Louis River enters Lake Superior in its western arm. Absorption

274   is fairly evenly distributed there between water, phytoplankton, and CDOM, with some

275   contributions of NAP in May. By June and July, the surface waters are dominated by CDOM

276   and a growing contribution from phytoplankton. This is presumably due the spring melt entering

277   the lake. August sees declining overall absorption as this is a time of lower river flow, with a

278   greater transition toward phytoplankton dominance in September and October when fall storms

279   generate more run off and the river serves as a nutrient delivery conduit to the lake (Figure 3).

280   The surface waters of the central region of the lake remain dominated by water year-round with a

281   significant CDOM contribution near the Ontonagon River outlet and within the Keweenaw

282   Peninsula waterway that contains Portage Lake. Samples at mid-depth are not targeted when the

283   water column is well mixed in May and June. The mid-depth becomes progressively dominated

284   by phytoplankton between July and September as the DCM develops and declines. By October,

285   surface and mid-depth absorption are similar (Figure 3). Considering the absorption budget,

286   CDOM is by far the largest contributor (50-80%), followed by phytoplankton, while NAP makes

287   less than a 15% contribution across all stations. Phytoplankton make up a greater percentage of

288   mid-depth absorption, while CDOM is more variable in surface waters. NAP contributions are

289   only slightly less in the mid-depth (Figure 4).

290   To display the spectral variability observed in the absorption budget, three stations are

291   selected in different regions throughout the lake (Figure 5). As $a_{CDOM}(\lambda)$ absorbs most strongly

292   in the ultraviolet and blue region of the spectrum, its contribution decreases exponentially with

293   increasing wavelength. Phytoplankton also absorb strongly in the blue region of the spectrum,

294   with a peak near 443 nm and a secondary peak at 687 nm. While phytoplankton account for a

295   larger proportion of absorption at mid-depth compared to the surface, they comprise <50% of the

296   total absorption budget in blue wavelengths at all depths (Figure 5). NAP is a larger contributor

297   in the surface, particularly for the sites near river outlets (Figure 5 A, C).

298   The particulate portion of absorption (NAP and phytoplankton) can be further explored

299   by SPM_i and SPM_o. $a_{NAP}(\lambda)$ includes all non-phytoplankton particles, while SPM_i includes only

300   minerogenic particles. Similar to absorption, greatest SPM loads are found near the outlet of the

301   St. Louis River with magnitude varying with season (Figure 6). The high volumes of spring melt

302   also delivered or stimulated growth resulting in high SPM_o in June. By July, freshwater entering

303   the lake from the river is warm enough to cause a density gradient, where the warm river water

304   sat on top of the colder lake water; thus, SPM is significantly lower at the mid-depth. In August,

305   SPM magnitude is relatively similar across the lake and between surface and mid-depth but

306   SPM_i contributed a greater proportion of SPM at depth. By September and October, the depth

307   distribution of SPM_i and SPM_o are similar, but the magnitude of SPM in the western arm is

308   much greater in October due to runoff and water column mixing from fall storms. At this time of

309   year, the riverine water is cooling faster than the lake, resulting in a submerged river plume; thus

310   greatest SPM is observed in the mid-depth.

311   In addition to the discreet measurements, *in situ* profiles of $a_p(\lambda)$, $a_{CDOM}(\lambda)$ and $b_{bp}(\lambda)$ are

312   collected. Figure 7 displays examples of this spectral data for the same three stations as in

313   Figure 5. The St. Louis River inflow in the western basin is seen in $a_p(\lambda)$ in the surface of the

314   water column (Figure 7A), and the DCM at mid-depth. The presence of the phytoplankton in

315    $a_p(\lambda)$ is evident by a secondary spectral peak near 683 nm. Riverine impact is also seen where

316    $a_{CDOM}(\lambda)$ is elevated in the near-surface waters but slightly deeper than $a_p(\lambda)$, due to CDOM

317   photobleaching (Figure 7B). In the Ontonagon Outflow, the riverine signal is also seen in $a_p(\lambda)$

318   and $a_g(\lambda)$, with a large deep chlorophyll contribution to $a_p(\lambda)$ at mid-depth. $a_{CDOM}(\lambda)$ is elevated

319   below the deep chlorophyll layer, possibly from bloom degradation and sinking (Figures 7 C, D).

320   Along the South Shore, there is no significant riverine source, thus $a_p(\lambda)$ is low in the surface and

321   high at depth associated with the DCM. $a_{CDOM}(\lambda)$ is uniform throughout the water column and

322   significantly lower than the riverine impacted sites (Figures 7 E, F). Spectra are extracted from

323   the profiles at 5 m and 25 m to show an alternative view of the spectral site comparison. Given

324   the low contribution of $a_{NAP}(\lambda)$ to the overall absorption budget (Figure 5), variability in the

325   spectral shape of *in situ* $a_p(\lambda)$ can be generally attributed to differences in the phytoplankton

326   community between the three locations (Figures 7 G, H). The most distinct difference is the

15

327   presence of a peak at green wavelengths (centered at 550 nm) for the location in the western

328   basin, which is not present at the other two sites. The variability in the slope of $a_{CDOM}(\lambda)$ is

329   related to the molecular weight of the source carbon (Helms et al., 2008). The slopes of

330    $a_{CDOM}(\lambda)$ are slightly lower at 5 m than 25 m suggesting proportionately more terrestrial material

331   in surface waters than water at depth (Figures 7 I, J). $b_{bp}(\lambda)$ magnitude indicates the amount of

332   particulate matter in the water, while the slope is related to the size of the particles, with steeper

333   slopes associated with smaller particles (Reynolds et al., 2001). The magnitude of $b_{bp}(\lambda)$ at 5 m

334   is directly proportional to the particle delivery to that location, with the St. Louis River, followed

335   by the Ontonagon River outflow, contributing significant particle loads. The $b_{bp}(\lambda)$ of the

336   western basin and the South Shore are nearly identical at 25 m suggesting a similar size of

337   phytoplankton at these locations. The $b_{bp}(\lambda)$ at the Ontonagon outflow at 25 m is higher and had

338   a greater slope, suggesting a greater abundance of phytoplankton and also a different community

339   composition (Figure 7 K, L).

340   Absorption and scattering processes impact the underwater light field as well as light

341   exiting the water column (i.e. $R_{rs}(\lambda)$). $R_{rs}(\lambda)$ is the parameter that a satellite radiometer observes.

342   Figure 8 displays $R_{rs}(\lambda)$ from in-water measurements at the surface, across all observation

343   months, and light field variability with depth for the three stations also highlighted in Figures 5

344   and 7. There are groups of similarly shaped $R_{rs}(\lambda)$, with peaks near 490 or 570 nm and varying

345   magnitudes (Figure 8 A-F). The magnitude of $R_{rs}(\lambda)$ is related to particulate abundance. The

346   shape of $R_{rs}(\lambda)$ is primarily related to the variations in the relative contributions and composition

347   of phytoplankton, NAP and CDOM. The spectra with the highest $R_{rs}(\lambda)$ are found in the St.

348   Louis River outflow. The underwater light field also varies spectrally depending on the

349   abundance and type of optical constituents. The spectrally dependent depth of light penetration

350   (i.e. $E_d(\lambda)$) as well as the spectral light at depth (ratio of $L_u(\lambda)$ to $E_d(\lambda)$), show significant

351   variability across the three example sites (Figure 8 G-L). The least amount of light is available

352   in the western basin with most available light at 510 nm, while light penetrates the deepest near

353   the South Shore and the most available light is at 490 nm. The diffuse attenuation coefficient at

354   490 nm ($K_d(490)$ is mapped to show geographic variability (Figure 9). The shortest attenuation

355   lengths (highest $K_d(490)$) are found in the western basin; the greatest lengths are found in the

356   central basin away from land in August.

357

358   **4. Conclusions**

359   This dataset has increased the coincident optical observations in Lake Superior from 8

360   observed in July 2006 (Effler et al., 2010) to 106 stations sampled during the ice-free season

361   (May through October) in 2013 to 2016. In addition to greatly expanding the temporal resolution

362   of available data, the spatial (geographic and depth) distribution has grown to cover the western

363   basin, central lake and the southern shore of the eastern basin. In a system that is challenging to

364   observe from direct methods for half the year due to prolonged winter conditions, remote sensing

365   is an important tool. The data presented here are essential for remote sensing algorithm

366   development and validation and this dataset will go a long way toward improving and ensuring

367   science quality satellite products are produced for the interpretation of lake processes.

368   Additionally, this dataset is valuable for characterizing the variable light field, particle,

369   phytoplankton, and colored dissolved organic matter distributions, and helpful in food web and

370   carbon cycle investigations, among others.

371

Open Access
Earth System
Science
Data
Discussions

5. Data Availability

The data set contains coincident observations of total, particulate, phytoplankton and CDOM absorption, total scatting, total and particulate backscattering, attenuation, remote sensing reflectance, chlorophyll concentration and total suspended matter from 106 stations, collected between 2013 and 2016. The compiled data are available from the National Aeronautics and Space Administration's SeaWiFS Bio-optical Archive and Storage System (SeaBASS): https://seabass.gsfc.nasa.gov/archive/URI/Mouw/LakeSuperior/ (Mouw et al., 2017).

Author Contributions. Mouw secured resources for the purchase of the optical instrumentation and funding supporting the effort and designed the sampling. Ciochetto maintained the optical instrumentation throughout the project period, quality controlled and achieved the dataset. While all authors contributed toward the fieldwork to collect the observations, Grunert and Ciochetto were responsible for the greatest amount of fieldwork. Ciochetto oversaw the laboratory sample analysis, processed all data and prepared figures. Mouw prepared the manuscript with contributions from all co-authors.

References

[APHA/AWWA/WEF] American Public Health Association, American Water Works
   Association and Water Environment Federation. 2005. Standard Methods for the
   Examination of Water and Wastewater, 21st Edition. Sections 2540A Solids, 2540C Total
   Suspended Solids Dried at 103-105°C and 2540E Fixed and Volatile Solids Ignited at 550°C.

Assel, R. A. 1986. Fall and winter thermal structure of Lake Superior. Journal of Great Lakes
   Research 12: 251–262, doi: 10.1016/S0380-1330(86)71725-5.

Austin, J. A., and J. Allen. 2011. Sensitivity of summer Lake Superior thermal structure to
   meteorological forcing. Limnology and Oceanography 56: 1141-1154.

Austin, J. A., and S. M. Colman. 2007. Lake Superior summer water temperatures are increasing
   more rapidly than regional air temperatures: A positive ice-albedo feedback. Geophysical
   Research Letters 34: L06604.

Barbiero, R. P., & M. L. Tuchman. 2001. Results from the U.S. EPA's biological open water
   surveillance program of the Laurentian great lakes: I. Introduction and Phytoplankton Results.
   Journal of Great Lakes Research, 27(2), 134–154.

Barbiero, R. P., and M. L. Tuchman. 2004. The Deep Chlorophyll Maximum in Lake Superior.
   Journal of Great Lakes Research 30: 256–268. doi:10.1016/S0380-1330(04)70390-1.

Boss, E., L. Taylor, S. Gilbert, K. Gundersen, N. Hawley, C. Janzen, T. Johengen, H. Purcell, C.
   Robertson, D.W.H. Schar, G.J. Smith and M.N. Tamburri. 2009. Comparison of inherent
   optical properties as a surrogate for particulate matter concentration in coastal waters.
   Limnology and Oceanography Methods, 7: 803-810.

Budd, J., and D. Warrington. 2004. Satellite-based sediment and chlorophyll a estimates for Lake
   Superior. Journal of Great Lakes Research 30: 459–466. doi:10.1016/S0380-1330(04)70406-
   2.

Dierssen, H. M. 2010. Perspectives on empirical approaches for ocean color remote sensing of
   chlorophyll in a changing climate. Proceedings of the National Academy of Sciences 107:
   17073–17078. doi:10.1073/pnas.0913800107.

Effler, S. W., M. Perkins, F. Peng, C. Strait, A. D. Weidemann, and M. T. Auer. 2010. Light-
   absorbing components in Lake Superior. Journal of Great Lakes Research 656–665.
   doi:10.1016/j.jglr.2010.08.001.

Helms, J., A. Stubbins, J. Ritchie, E. Minor, D. Kieber, and K. Mopper. 2008. Absorption
   spectral slopes and slope ratios as indicators of molecular weight, source, and photobleaching
   of chromophoric dissolved organic matter. Limnology and Oceangraphy 53: 955–969.

Hubbs, C. L., & K. F. Lagler. 2004. In G.R. Smith (Ed.), Fishes of the Great Lakes region
   (revised ed.). University of Michigan Press rev.

Lee, Z., K. Carder, and R. Arnone. 2002. Deriving inherent optical properties from water color: a
   multiband quasi-analytical algorithm for optically deep waters. Applied Optics 41: 5755–
   5772.

Lenters, J.D. 2004. Trends in the Lake Superior water budget since 1948: a weakening seasonal
   cycle. Journal of Great Lakes Research 30, Supplement 1: 20-40.

Li, H., J.W. Budd, and S. Green. 2004. Evaluation and regional optimization of bio-optical
   algorithms for Central Lake Superior. Journal of Great Lakes Research, 30(1), 443–458.

Lohrenz, S. 2000. A novel theoretical approach to correct for pathlength amplification and
   variable sampling loading in measurements of particulate spectral absorption by the
   quantitative filter technique. Journal of Plankton Research 22: 639.

443   Lohrenz, S.E., A.D. Weidemann and M. Tuel. 2003. Phytoplankton spectral absorption
444   influenced by community size structure and pigment composition. Journal of Plankton
445   Research. 25(1): 35-61.
446   Mason, L. A., C. M. Riseng, A. D. Gronewold, E. S. Rutherford, J. Wang, A. Clites, S. D. P.
447   Smith, and P. B. McIntyre. 2016. Fine-scale spatial variation in ice cover and surface
448   temperature trends across the surface of the Laurentian Great Lakes. Climatic Change 1–13.
449   doi:10.1007/s10584-016-1721-2.
450   Matheson, D. H., & M. Munawar. 1978. Lake Superior Basin and its development. Journal of
451   Great Lakes Research, 4, 249–263.
452   Mobley, C. D. (1994), *Light and Water: Radiative Transfer in Natural Waters*, 592 pp.,
453   Academic, San Diego, California.
454   Mouw, C. B., H. Chen, G. A. McKinley, S. Effler, D. O'Donnell, M. G. Perkins, and C. Strait.
455   2013. Evaluation and optimization of bio-optical inversion algorithms for remote sensing of
456   Lake Superior's optical properties. Journal of Geophysical Research-Oceans 118: 1696–1714.
457   doi:10.1002/jgrc.20139.
458   Mouw, C.B., A.B. Ciochetto, B. Grunert, and A. Yu. (2017) LakeSuperior. SeaWiFS Bio-optical
459   Archive and Storage System (SeaBASS), NASA.
460   https://seabass.gsfc.nasa.gov/archive/URI/Mouw/LakeSuperior/.
461   Mouw, C. B., S. Greb, D. Aurin, and others. 2015. Aquatic color radiometry remote sensing of
462   coastal and inland waters: Challenges and recommendations for future satellite missions.
463   Remote Sensing of Environment 160: 15–30. doi:10.1016/j.rse.2015.02.001.
464   Mueller, J.L., G.S. Fargion and C.R. McClain. 2003a. Ocean optics protocols for satellite ocean
465   color sensor validation, revision 4, volume III: Radiometric Measurements and Data Analysis
466   protocols.   NASA/TM-2003-21621/Rev4-Vol.III.   National   Aeronautical   and   Space
467   Administration, Goddard Space Flight Space Center, Greenbelt, Maryland. 84 pp.
468   Mueller, J.L., G.S. Fargion and C.R. McClain. 2003b. Ocean optics protocols for satellite ocean
469   color sensor validation, revision 4, volume IV: Inherent Optical Properties: Instruments,
470   characterizations, field measurements and data analysis protocols. NASA/TM-2003-
471   211621/Rev4-Vol. IV. National Aeronautical and Space Administration, Goddard Space
472   Flight Space Center, Greenbelt, Maryland. 76 pp.
473   Munawar, M., & I.F. Munawar. 1973. Phytoplankton of Lake Superior. Journal of Great Lakes
474   Research, 4, 415–442.
475   O'Donnell, D. M., S. W. Effler, C. M. Strait, F. Peng, and M. Perkins. 2013. Remote sensing
476   reflectance in the Great Lakes: In situ measurements, closure analyses, and a forward model.
477   Journal of Great Lakes Research 39: 137–150. doi:10.1016/j.jglr.2013.06.016.
478   O'Reilly, C. M. and others 2015. Rapid and highly variable warming of lake surface waters
479   around the globe. Geophysical Research Letters: 2015GL066235.
480   Peng, F., S. Effler, D. O'Donnell, A. Weidemann, and M. Auer. 2009. Characterizations of
481   minerogenic particles in support of modeling light scattering in Lake Superior through a two-
482   component approach. Limnology and Oceanography 54: 1369–1381.
483   Pope, R.M. and E.S. Fry. 1997. Absorption spectrum (380-700nm) of pure water. II. Integrating
484   cavity measurements. Applied Optics: 18, 8710-8723.
485   Reynolds, R., D. Stramski, and B. Mitchell. 2001. A chlorophyll-dependent semianalytical
486   reflectance model derived from field measurements of absorption and backscattering
487   coefficients within the Southern Ocean. Journal of Geophysical Research 106: 7125–7138.

488 Smith, R.C., and K.S. Baker. 1984. Analysis of ocean optical data. In M. Blizard, Ed., Ocean
489   Optics VII, SPIE, 478: 119-126.
490 Smith, R.C., and K.S. Baker. 1986. Analysis of ocean optical data. In P.N. Slater, Ed., Ocean
491   Optical VIII, SPIE, 637: 95-107.
492 Sterner, R. 2011. C:N:P stoichiometry in Lake Superior: freshwater sea as end member. Inland
493   Waters, 1(1), 29–46.
494 Sterner, R. W. 2010. In situ-measured primary production in Lake Superior. Journal of Great
495   Lakes Research, 36(1), 139–149.
496 Sullivan, J.M., M.S. Twardowski, J.R.V. Zaneveld, C.M. Moore, A.H. Barnard, P.L. Donaghay
497   and B. Rhoades. 2006. Hyperspectral temperature and salt dependencies of absorption by
498   water and heavy water in the 400-750 nm spectral range. Applied Optics 45(21): 5294-5309.
499 Sullivan, J.M., M.S. Twardowski, J.R.V. Zaneveld and C.C. Moore. 2013. Measuring optical
500   backscattering in water. In: Kokhanovsky, A.A. [Ed.] Light Scattering Reviews 7: Radiative
501   Transfer and Optical Properties of Atmosphere and Underlying Surface. Springer Praxis
502   Books. doi: 10.1007/978-3-642-21907-8_6. Chapter 6, pp 189-224.
503 Tassan, S. and G.M. Ferrari. 2002 A sensitivity analysis of the "Transmittance-Reflectance"
504   method for measuring light absorption by aquatic particles. Journal of Plankton Research.
505   24(8): 757-774.
506 Trees, C.C., R.R. Bidigare, D.M. Karl, L.V. Heukelem and J. Dore. 2003. Fluorometeric
507   chlorophyll a: sampling, laboratory methods and data analysis protocols, In: Mueller, J.L.,
508   G.S. Fargion, and C.R. McClain [Eds.] Ocean Optics Protocols for Satellite Ocean Color
509   Sensor Validation, Revision 5, Volumne V: Biogeochemical and Bio-optical measurements
510   and data analysis protocols. NASA/TM-2003-211621, NASA Goddard Space Flight Center,
511   Greenbelt, MD, Chapter 3, pp 15-25.
512 Trochta, J. T., C. B. Mouw, and T. S. Moore. 2015. Remote sensing of physical cycles in Lake
513   Superior using a spatio-temporal analysis of optical water typologies. Remote Sensing of
514   Environment 171: 149–161. doi:10.1016/j.rse.2015.10.008.
515 Weller, R. R. (1978). Chemistry of Lake Superior. Journal of Great Lakes Research, 4, 370–385.
516 Woźniak, S.B., J. Meler, B. Lednicka, A. Zdun, J. Stoń-Egiert. 2011. Inherent optical properties
517   of suspended particulate matter in the southern Baltic Sea. Oceanologia, 53(3): 691-729.
518   doi:10.5697/oc.53-3.691.
519 Zaneveld, J.R.V., J.C. Kitchen and C. Moore. 1994. The scattering error correction of reflecting-
520   tube absorption meters. Ocean Optics XII, Proc. SPIE, 2258: 44-55.
521 Zhang, X. and L. Hu. 2009 Estimating scattering of pure water from density fluctuations of the
522   refractive index. Optics Express: 17(3): 1671-1678.
523
524

525 **Table 1.** Summary of parameters.
526
527 **Found in Dataset**
528     $a_{nw}(\lambda)$ spectral non-water absorption (m^{-1})
529     $a_p(\lambda)$ spectral particulate absorption (m^{-1})
530     $a_{ph}(\lambda)$ spectral phytoplankton absorption (m^{-1})
531     $a_{NAP}(\lambda)$ spectral non-algal particle absorption (m^{-1})
532     $a_{CDOM}(\lambda)$ spectral colored dissolved organic matter absorption (m^{-1})
533     $b_b(\lambda)$ spectral total backscattering (m^{-1})
534     $b_{bp}(\lambda)$ spectral particulate backscattering (m^{-1})
535     $c_{nw}(\lambda)$ spectral non-water attenuation (m^{-1})
536     $E_d(\lambda)$ downwelling irradiance $(\mu W\ cm^{-2})$
537     $E_s(\lambda)$ surface irradiance $(\mu W\ cm^{-2})$
538     $L_u(\lambda)$ upwelling radiance $(\mu W\ cm^{-2}\ sr^{-1})$,
539   [Chl]   chlorophyll *a* concentration $(mg\ m^{-3})$
540   [Pheo]   pheopigment concentration $(mg\ m^{-3})$
541   SPM   total suspended particulate matter $(mg\ L^{-1})$
542   SPM_i inorganic suspended particulate matter $(mg\ L^{-1})$
543   SPM_o organic suspended particulate matter $(mg\ L^{-1})$
544
545 **Not in Dataset, but used in Calculations**
546     $a_t(\lambda)$ spectral total absorption (m^{-1})
547     $a_w(\lambda)$ spectral water absorption (m^{-1})
548     $b_t(\lambda)$ spectral total scattering (m^{-1})
549     $b_w(\lambda)$ spectral water scattering (m^{-1})
550     $b_{bw}(\lambda)$ spectral water backscattering (m^{-1})
551     $c_t(\lambda)$ spectral total attenuation (m^{-1})
552     $L_w(\lambda)$ water-leaving radiance $(\mu W\ cm^{-2}\ sr^{-1})$
553     $R_{rs}(\lambda)$ spectral remote sensing reflectance (sr^{-1})
554     $R(\lambda)$ spectral reflectance (sr^{-1})
555     $K_d(\lambda)$ spectral downwelling diffuse attenuation coefficient (m^{-1})
556     $K_u(\lambda)$ spectral upwelling diffuse attenuation coefficient (m^{-1})
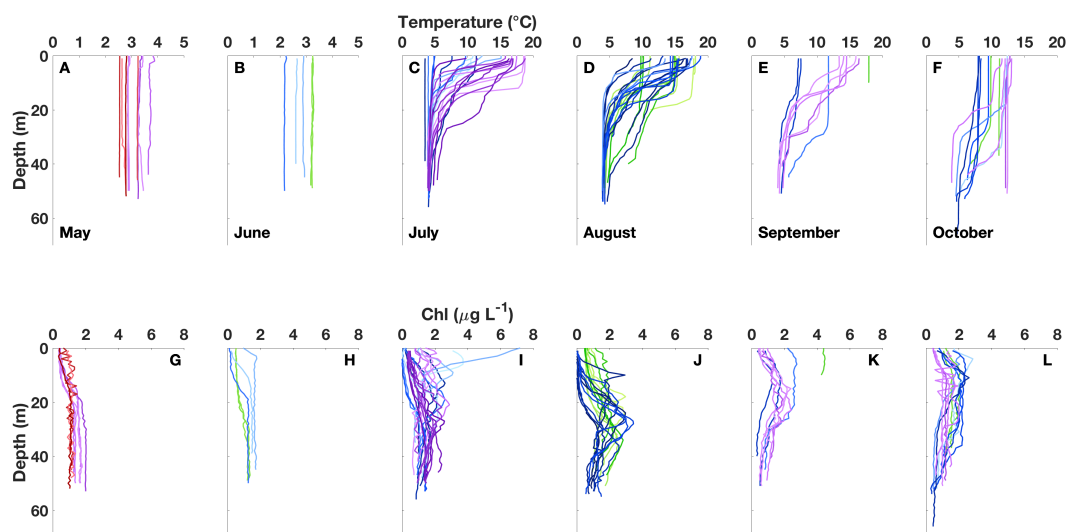557
558

559
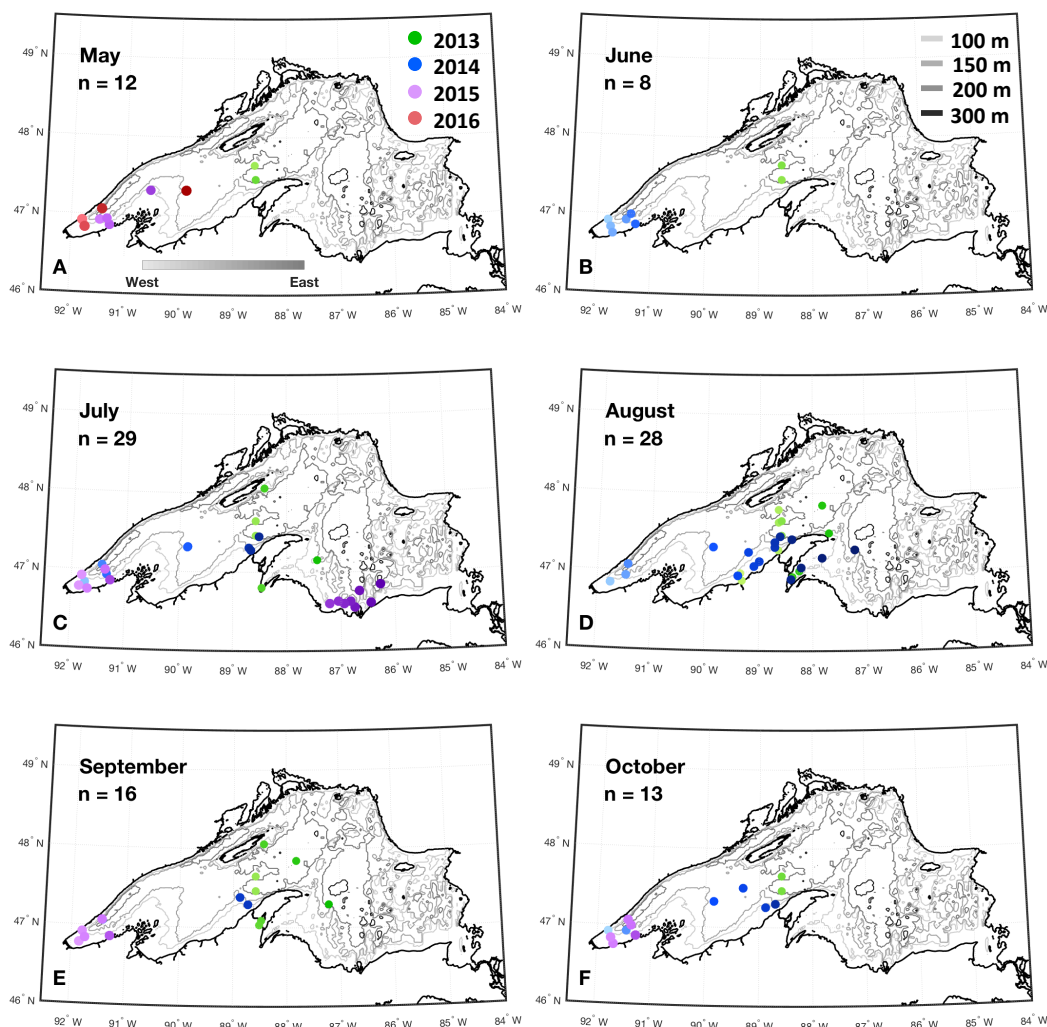
560
561
562 **Figure 1.** Station locations for the Lake Superior dataset sampled between 2013-2016 and
563 grouped by month. Locations are colored by year and shaded by longitude from dark to light
564 running east to west as shown in the legend (A). Depth contours shown in grey.
565

566
567
Figure 2. Profiles of temperature (A-F) and [Chl] retrieved from *in situ* fluorescence (G-L) for the Lake Superior dataset. Profiles are colored by year and shaded by longitude as in Figure 1. Data are binned by 1-m. Note compressed x-axis limits for temperature profiles in May and June (A-B). Throughout the region, water column stratification is not observed until July or even August (C-D) and is eroded in the fall (F). Absolute [Chl] levels are low throughout the lake, even during spring and summer months (G-L).
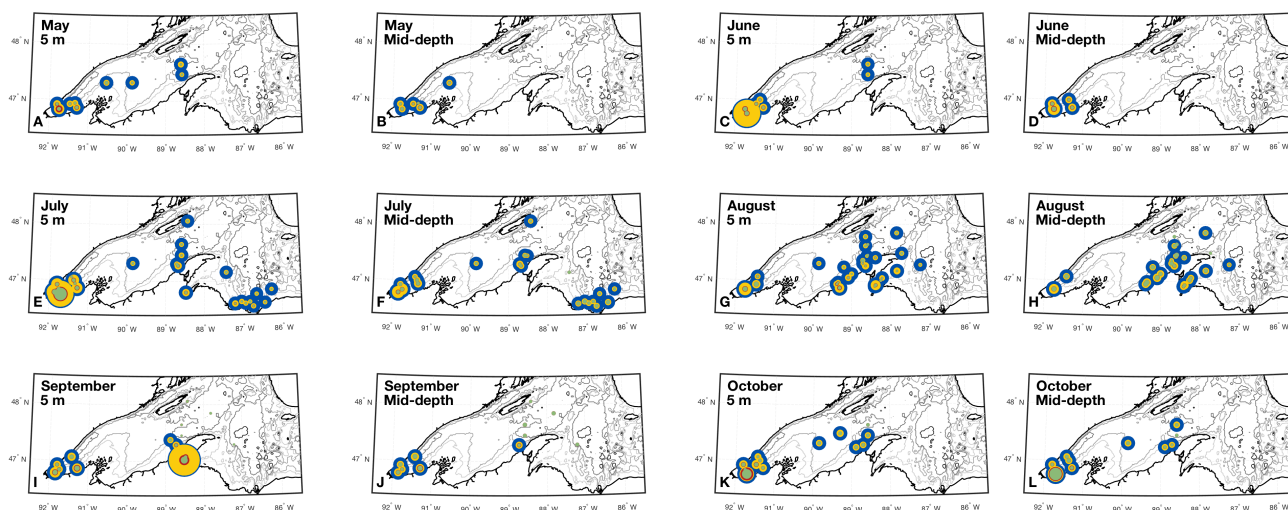
Figure 3. Absorption for discrete water samples taken at 5m and mid-depth throughout Lake Superior grouped by month. The outer diameter for each station marker is relative to total absorption with the contribution of water, CDOM, non-algal particles and phytoplankton indicated by the relative size of concentric circles.

580
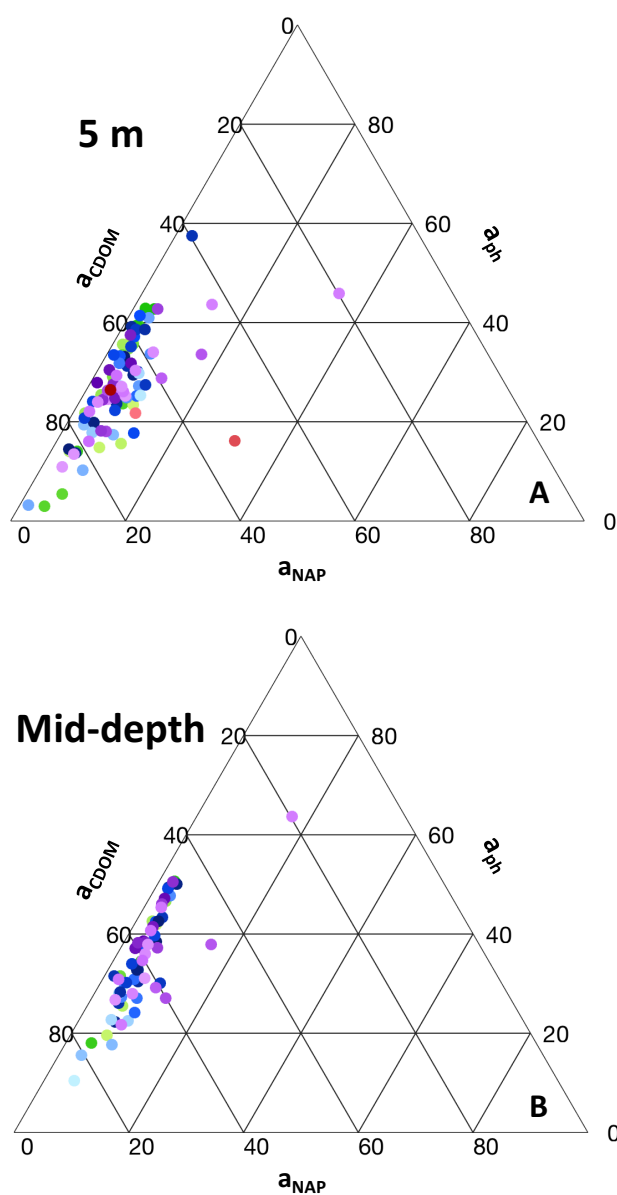
581
582
583 **Figure 4.** Ternary plots of the contribution of CDOM, non-algal particles and phytoplankton to
584 total non-water absorption at 443 nm from discrete water samples taken at 5m (A) and mid-depth
585 (B). Markers are colored by year and shaded by longitude as in Figure 1. The system is CDOM
586 dominated, especially near the surface; phytoplankton contributed more than 50% in only 2 cases
587 for the entire dataset.
588
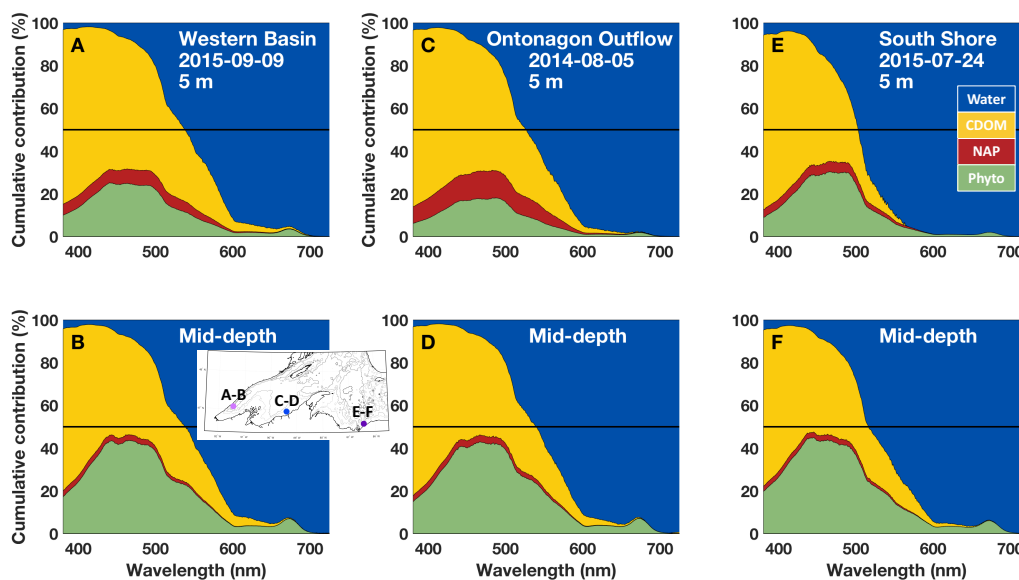
Figure 5. Spectrally resolved contribution of water, CDOM, non-algal particles and phytoplankton to total absorption for discrete water samples taken at 5m (A, C, E) and at mid-depth (B, D, F) from the Western Basin (A-B, light purple marker on map inset in B), Ontonagon River Outflow (C-D, blue marker on map) and South Shore (E-F, dark purple marker on map) of Lake Superior in the summer of 2014-2015. Black lines indicate 50% cumulative contribution for visual reference.
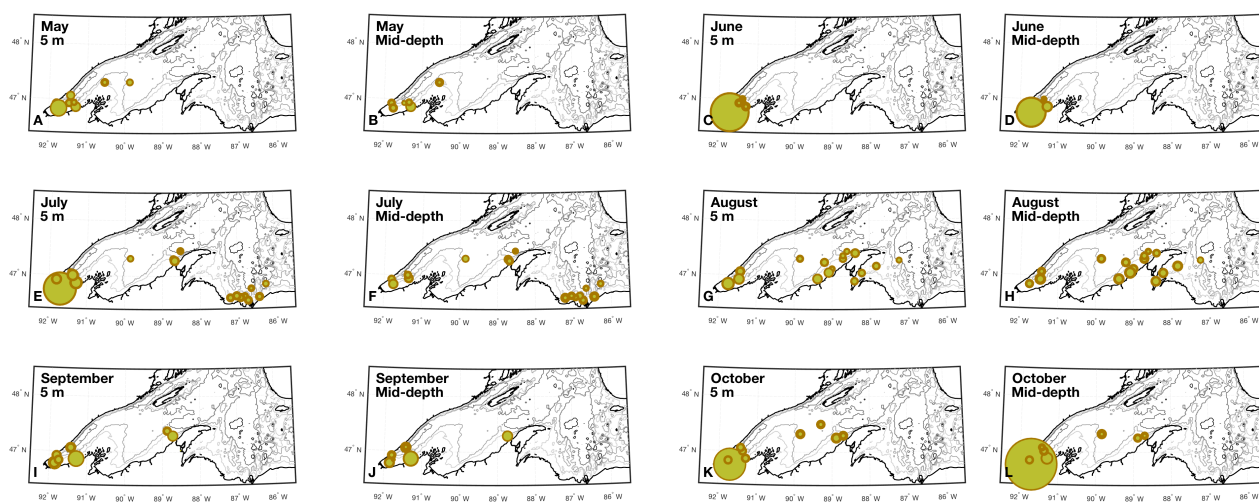
597
598
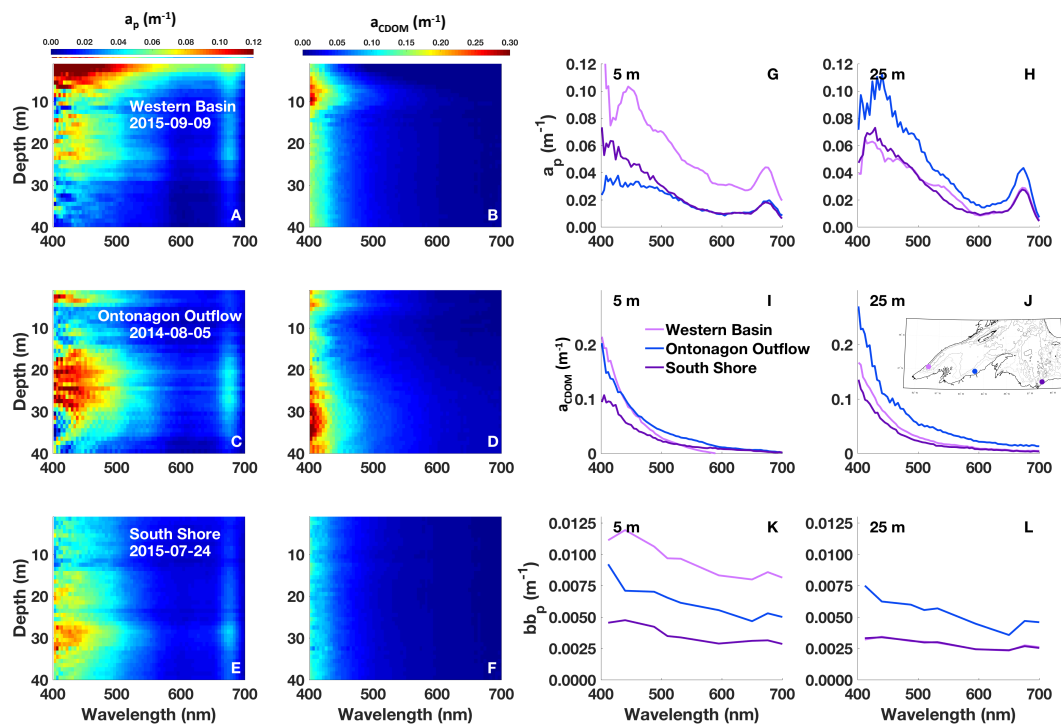599 **Figure 6.** Suspended particulate matter for discrete water samples taken at 5m and mid-depth for the Lake Superior dataset grouped
600 by month. The outer diameter of each station marker indicates total SPM with concentric circles representing the relative contributions
601 of organic and inorganic components.

602

603
604
605 **Figure 7.** *In situ* IOP for select stations throughout Lake Superior in the summer of 2014 and
606 2015 (see inset map in J). Profiles of $a_p(\lambda)$ (A, C, E) and $a_{CDOM}(\lambda)$ (B, D, F) for the Western Basin
607 (A-B), Ontonagon River Outflow (C-D) and South Shore (E-F). Note different color scales for
608 $a_p(\lambda)$ and $a_{CDOM}(\lambda)$ profiles. Examples of individual spectra at 5m and 25m are shown in G-J
609 along with *in situ* particulate backscattering (K-L). Data are binned to 1-m.
610
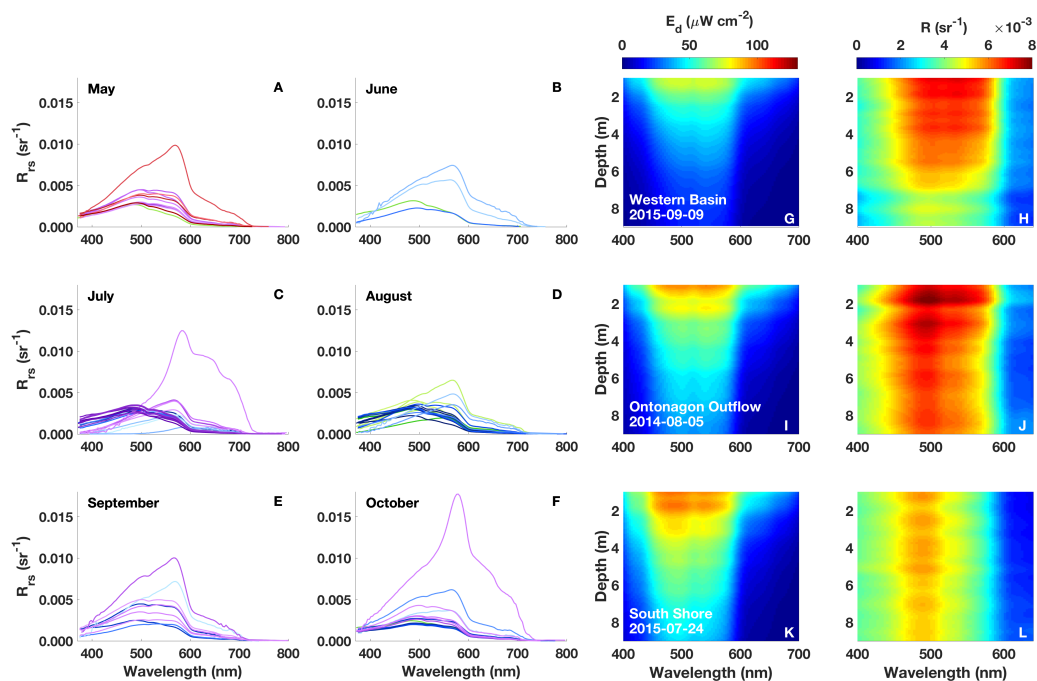
611
612
613 **Figure 8.** $R_{rs}(\lambda)$ ($=L_w(\lambda)/E_s(\lambda)$) retrieved from combined near-surface multi-cast AOP profiles
614 (A-F). Spectra are colored by year and shaded by longitude as in Figure 1. Example spectral
615 multi-cast AOP profiles for downwelling irradiance ($E_d(\lambda)$) and reflectance ($R(\lambda)=L_u(\lambda)/E_d(\lambda)$)
616 for the three locations from Figures 5 and 7 (G-L).
617
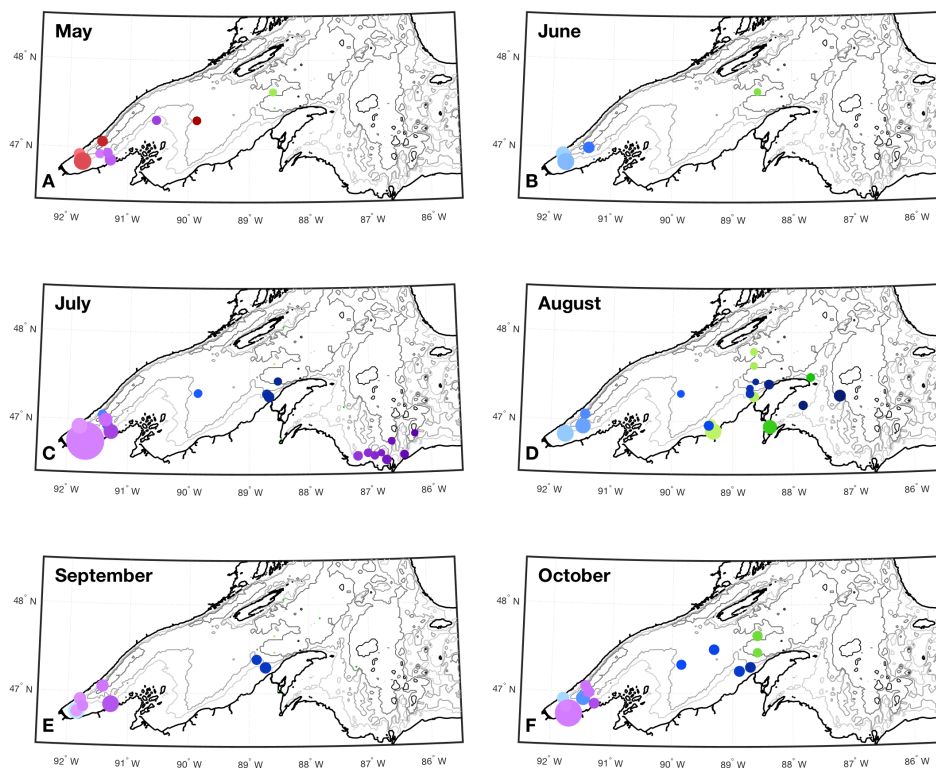
618
619
620 **Figure 9.** $K_d(490)$ (m^{-1}) for the Lake Superior dataset grouped by month. Stations are colored by
621 year and shaded by longitude as in Figure 1.
622